Mesoscale Defect Motion in Binary Systems: Effects of Compositional Strain and Cottrell Atmospheres

Marco Salvalaglio,[1,2,*] Axel Voigt,[1,2] Zhi-Feng Huang,[3] and Ken R. Elder[4]
[1]Institute of Scientific Computing, TU Dresden, 01062 Dresden, Germany
[2]Dresden Center for Computational Materials Science, TU Dresden, 01062 Dresden, Germany
[3]Department of Physics and Astronomy, Wayne State University, Detroit, Michigan 48201, USA
[4]Department of Physics, Oakland University, Rochester, Michigan 48309, USA

(Received 18 January 2021; revised 6 April 2021; accepted 7 April 2021; published 6 May 2021)

The velocity of dislocations is derived analytically to incorporate and predict the intriguing effects induced by the preferential solute segregation and Cottrell atmospheres in both two-dimensional and three-dimensional binary systems of various crystalline symmetries. The corresponding mesoscopic description of defect dynamics is constructed through the amplitude formulation of the phase-field crystal model, which has been shown to accurately capture elasticity and plasticity in a wide variety of systems. Modifications of the Peach-Koehler force as a result of solute concentration variations and compositional stresses are presented, leading to interesting new predictions of defect motion due to effects of Cottrell atmospheres. These include the deflection of dislocation glide paths, the variation of climb speed and direction, and the change or prevention of defect annihilation, all of which play an important role in determining the fundamental behaviors of complex defect network and dynamics. The analytic results are verified by numerical simulations.

DOI: 10.1103/PhysRevLett.126.185502

In crystalline systems, topological defects, such as dislocations and grain boundaries, play a significant role in controlling system properties. For example, in polycrystals, the average grain size plays a major role in determining the magnitude of the magnetic coercivity [1,2], yield stress [3,4], and thermal conductivity [5]. It is, thus, of critical importance to understand the nature of defect motion and the corresponding elastoplastic mechanisms during the evolution of nonequilibrium material systems, which control, e.g., grain coarsening rates and, hence, the resulting defected structures and configurations of polycrystalline systems. Dislocations lead to strains in crystalline lattices which, in turn, are offset to some extent in binary alloys by phase segregation, or *Cottrell atmospheres* [6–8] near the dislocation cores. This segregation influences the motion of dislocations and grain boundaries [9–13] by modifying the effective Peach-Koehler driving force that acts on the dislocations. Typically, this phenomenon was investigated by focusing on concentration profiles and stress distribution around dislocations [14–17] and the force-velocity curves for defect motion. In most cases, either continuum modeling of defect motion or atomistic description was considered. This also applies to computational studies, from the first numerical approaches tracking concentration profiles and velocities [18,19] up to the most recent advanced numerical investigations accounting for segregation at both dislocations [20–22] and grain boundaries [23–25].

Given the complex, mesoscopic characteristics of the defect motion, it is of fundamental importance to bridge the above two ends of the description spectrum at atomistic and long-wavelength continuum scales and examine the key features of mesoscale effects [26]. This often requires coarse-grained approaches, handling large length scales through continuum density fields that still retain relevant microscopic details of the atomic structures of defects. Although much progress has been made on this front, such as those based on the multiscale phase-field crystal (PFC) method [27–29], most studies have been focused on the defect dynamics in single-component systems [30–33], while the understanding of the defect behavior in alloys or multicomponent systems, especially the novel elastoplastic properties originated from the coupling to compositionally generated effects, is still limited.

In this Letter, we construct a mesoscopic description of dislocation dynamics for binary alloy systems, through an analytic formulation of dislocation velocities as a function of the solute expansion coefficient and alloy concentration (i.e., compositional strain), for various two-dimensional (2D) and three-dimensional (3D) crystalline symmetries. It is based on the PFC model in its complex amplitude expansion formalism (APFC) [32,34–37] and extends the current description of defect velocities in 2D single-component systems for triangular lattices [30] to incorporate the key effects induced by local concentration variations around defects in both 2D and 3D binary systems. The mesoscale character of this framework results

from the coarse-grained description of the lattice structure, deformation fields, and variations of the alloy concentration conveyed by the APFC model, although dislocations are still described as individual objects rather than through an averaged dislocation density. Numerical APFC simulations are used to verify the analytic calculations, illuminating the solute preferential segregation at defects and, importantly, its influence on defect motion for different configurations and crystal symmetries. One of the intriguing results is the prediction of the deflection of dislocations from the glide paths and the change of climb direction that would be followed in a pure system. This could even prevent defect annihilation, indicating the novel effect of Cottrell atmospheres and the compositionally induced stress on defect dynamics.

The original binary PFC model [29] is formulated in terms of the dimensionless atomic number density variation field $\varrho(\vec{r},t)$ and a solute concentration field $\psi(\vec{r},t)$. For the purposes of this work, it is useful to consider the corresponding amplitude expansion representation [36], in which the density field is expanded by

$$\varrho = \sum_n \eta_n e^{i\vec{q}_n\cdot\vec{r}} + \text{c.c.}, \tag{1}$$

where $\eta_n(\vec{r},t)$ are complex, slowly varying amplitudes, the wave vectors $\vec{q}_n$ specify a given crystalline symmetry, "c.c." represents the complex conjugate, and, for simplicity, the average of ϱ is set as constant and zero. By assuming the lattice spacing R to be linearly proportional to ψ (Vegard's law), we have $R = R_0(1+\alpha\psi)$ with α the solute expansion coefficient. The dynamic equations for n and ψ in dimensionless form are written as [38]

$$\frac{\partial\eta_n}{\partial t} = -q_n^2\frac{\partial F}{\partial\eta_n^*}, \qquad \frac{\partial\psi}{\partial t} = \nabla^2\frac{\partial F}{\partial\psi}, \tag{2}$$

respectively, where

$$\begin{aligned} F = \int\Bigg[&\frac{\Delta B_0}{2}\Phi + \frac{3v}{4}\Phi^2 + \sum_n\left(B_0^x|\mathcal{G}_n\eta_n|^2 - \frac{3v}{2}|\eta_n|^4\right) \\ &+ f^s(\{\eta_n\}) + (\omega + B_2^l\Phi)\frac{\psi^2}{2} + \frac{u}{4}\psi^4 \\ &- 2B_0^x\alpha\sum_n q_n^2(\eta_n\mathcal{G}_n^*\eta_n^* + \text{c.c.})\psi\Bigg]d\vec{r}, \end{aligned} \tag{3}$$

$\Phi = 2\sum_n|\eta_n|^2$, $\mathcal{G}_n = \nabla^2 + 2i\vec{q}_n\cdot\vec{\nabla}$, and ΔB_0, v, B_0^x, w, B_2^l, and u are model parameters as described in Ref. [29]. Here, $f^s(\{\eta_n\})$ is a polynomial in η_n (and η_n^*) that depends on the specific crystalline symmetry under consideration (see Supplemental Material [39]). It can be shown that, given $\vec{q}_n$ the basic wave vectors corresponding to a pure system, the equilibrium wave vectors for binary systems read $\vec{q}_n^{\,\text{eq}} = \vec{q}_n\sqrt{1-2\alpha\psi}$ [37]. This amplitude model as written does not impose instantaneous mechanical equilibrium, nor does it contain Peierls barriers to defect motion, although both effects have been included in more complex models [31,33,41].

A dislocation in a crystalline lattice corresponds to a discontinuity in the phase (θ_n) of the complex amplitudes which can be written as $\eta_n = \phi_n e^{i\theta_n}$. The discontinuity in the phase corresponds to a discontinuity in the displacement field $\vec{u}$ that enters continuum elasticity theory, since this displacement is equivalent to setting $\theta_n = -\vec{q}_n\cdot\vec{u}$ [36,42]. More explicitly, a dislocation with Burgers vector $\vec{b}$ is defined by $\oint d\vec{u} = \vec{b}$, corresponding to $\oint d\theta_n = -\vec{q}_n\cdot\vec{b} = -2\pi s_n$, where s_n is the winding number. As in Ref. [30], in what follows the vortex solution $\eta_n \propto x - is_n y$ will be considered with $s_n = \pm 1$.

To examine the influence of solute concentration on dislocation motion, it is useful to define the Burgers vector density $\vec{B}(\vec{r})$ as $\vec{B}(\vec{r}) = \sum_m \vec{b}_m\delta(\vec{r}-\vec{r}_m)$, where $\vec{b}_m$ and $\vec{r}_m$ are the Burgers vector and position of the mth dislocation, respectively. At a dislocation core, some of the amplitudes go to zero; it is, thus, useful to make a transformation from spatial coordinates to the real and imaginary components of the complex amplitudes. Generalizing Ref. [30] to the case of a point dislocation in 2D or an edge dislocation in 3D, the transformation leads to

$$\vec{B} = -\beta\sum_n \vec{q}_n D_n\delta(\eta_n), \qquad D_n = \frac{\varepsilon_{jk}}{2i}\partial_j\eta_n\partial_k\eta_n^*, \tag{4}$$

where $\beta = 2\pi/\sum(q_j^n)^2$ for $j = x, y, z$, ε_{jk} is the Levi-Civita symbol, and the Einstein summation convention is implied. By writing $\vec{B}$ in terms of the amplitudes, the dynamics of $\vec{B}$ is determined by

$$\frac{\partial B_i}{\partial t} = -\partial_j\mathcal{J}_{ij} = -\partial_j\left[\sum_m b_i^m v_j^\alpha\delta(\vec{r}-\vec{r}_m)\right], \tag{5}$$

with the dislocation velocity

$$v_j^m = \frac{\beta}{2\pi}\sum_n\frac{(\vec{q}_n\cdot\vec{b}_m)^2}{|\vec{b}_m|^2}\frac{J_j^n}{D_n}, \qquad J_j^n = \varepsilon_{jk}\text{Im}(\dot{\eta}_n\partial_k\eta_n^*). \tag{6}$$

Near the dislocation core, the dynamic equation of motion for η_n can be approximated as

$$\frac{\partial\eta_n}{\partial t} = -q_n^2B_0^x[\mathcal{G}_n^2\eta_n - 2\alpha q_n^2(\psi\mathcal{G}_n\eta_n + \mathcal{G}_n\eta_n\psi)], \tag{7}$$

which can be further simplified to

$$\frac{\partial\eta_n}{\partial t} = -i8q_n^2B_0^x\vec{q}_n\cdot\vec{\nabla}\phi_n(\vec{q}_n\cdot\vec{\nabla}\theta_n + q_n^2\alpha\delta\psi)e^{i\theta_n}, \tag{8}$$

with $\delta\psi = \psi - \psi_{\text{core}} \approx \bar{\psi} - \psi_{\text{core}}$, i.e., the difference between the concentration far away from the dislocation

and its value at the defect core, where $\bar{\psi}$ is the average concentration. Substituting Eq. (8) into Eq. (6) and using the results $i\partial_j\eta_n = -1/s_n\varepsilon_{jk}\partial_k\eta_n$ and $\mathrm{Im}(\partial_j\eta_n\partial_k\eta_n^*) = \varepsilon_{jk}D_n$ [30] leads to

$$\frac{J_j^n}{D_n} = \frac{8}{s_n} q_n^2 B_0^x \varepsilon_{jk} q_k^n (q_l^n q_p^n \partial_l u_p - q_n^2 \alpha\delta\psi), \tag{9}$$

and, in turn,

$$v_j^m = \frac{8\beta B_0^x b_i^m}{|\vec{b}_m|^2}\varepsilon_{jk}\sum_n q_n^2 q_i^n q_k^n (q_l^n q_p^n \partial_l u_p - q_n^2\alpha\delta\psi). \tag{10}$$

Furthermore, since Eq. (10) is symmetric in l and p, it can be written in terms of the strain tensor $U_{ij} = (\partial_i u_j + \partial_j u_i)/2$ as follows:

$$v_j^m = \frac{8\beta B_0^x b_i^m}{|\vec{b}_m|^2}\varepsilon_{jk}\sum_n q_n^2 q_i^n q_k^n (q_l^n q_p^n U_{lp} - q_n^2\alpha\delta\psi). \tag{11}$$

Equation (11) is consistent with the classical Peach-Koehler force [43], since the corresponding stress (σ_{ij}) is proportional to the strain, i.e., $\sigma_{jk} = \lambda_{jklm}U_{lm}$, where λ_{jklm} is the rank-four elastic modulus tensor [44]. More explicitly, the calculations reported in Ref. [30] can be easily extended to more complex crystal structures where the magnitude ϕ_n of the complex amplitudes η_n are not all the same in equilibrium, giving

$$\sigma_{jk} = 8B_0^x U_{lp}\sum_n \phi_n^2 q_j^n q_k^n q_l^n q_p^n. \tag{12}$$

Note that both Eqs. (11) and (12) are of mesoscopic nature, given the mesoscale amplitudes, displacements, and concentration variations. For the case of a 2D triangular lattice or a 3D bcc crystal, where it is possible to construct the lattice by retaining only one mode of the lowest order (with $q_n = 1$), the velocity takes the form

$$v_j^m = M\varepsilon_{jk}\left(\sigma_{ki}b_i^m - 4B_0^x\phi_0^2\alpha\delta\psi b_i^m\sum_n q_i^n q_k^n\right), \tag{13}$$

with a mobility $M = 2\beta/(\phi_0^2|\vec{b}_m|^2)$ and the equilibrium amplitude magnitude ϕ_0 of the lowest-order mode. The last term in Eqs. (11) and (13) accounts for the new contribution from the compositionally generated stress, as a result of the compositional strain ($\sim\alpha\psi$) arising from local concentration variations, particularly solute preferential segregation (Cottrell atmospheres) around defects. Thus, Eqs. (11) and (13) provide explicit predictions for the influence of solute concentration on dislocation motion for general crystalline symmetries and are the main results of this Letter.

In what follows, we consider the lowest-order mode expansion that is a good approximation of the full PFC models near melting and is exact for the APFC. A 2D triangular (T) or honeycomb lattice requires three reciprocal vectors, $\vec{q}_1 = \langle -\sqrt{3}/2, -1/2\rangle$, $\vec{q}_2 = \langle 0, 1\rangle$, and $\vec{q}_3 = -\vec{q}_1 - \vec{q}_2$, and, thus,

$$\begin{aligned} v_x &= \gamma[2U_{xy}b_x + (U_{xx} + 3U_{yy})b_y - 4\alpha\delta\psi b_y], \\ v_y &= -\gamma[2U_{xy}b_y + (3U_{xx} + U_{yy})b_x - 4\alpha\delta\psi b_x], \end{aligned} \tag{14}$$

where $\gamma \equiv 4\pi B_0^x/|\vec{b}_m|^2$. Explicit expressions for a point dislocation in 2D square lattice and an edge dislocation in 3D bcc and fcc systems are given in Supplemental Material [39].

To validate the above analytical results, we numerically integrate the amplitude Eqs. (2) and (3) for some representative cases. Here, we consider the system in the single-phase regime of the phase diagram and do not investigate the influence of dislocations on phase separation in a two-phase state [25]. The simulations exploit the finite element toolbox AMDiS [45,46] and build on the algorithms described in Refs. [47,48]. The initial concentration field is set to be uniform, i.e., $\psi(\vec{r}) = \bar{\psi}$. The initial conditions for amplitudes are set to encode a distortion of a relaxed crystal having equilibrium wave vectors $\vec{q}_n^{\,\mathrm{eq}}$. Details are reported in Supplemental Material [39].

We first consider an edge dislocation in a 2D triangular lattice, with Burgers vector $\vec{b} = (\pm b_x, 0)$ and $b_x = a_{\mathrm{tri}} = 4\pi/\sqrt{3}$, forming between regions with opposite deformation u_x and corresponding to an equilibrium configuration in a pure system where no motion is expected with zero Peach-Koehler force. The solute segregation near defect cores is illustrated in Fig. 1, showing the $\psi(\vec{r})$ profiles computed. For $\bar{\psi} = 0$, two lobes with positive and negative $\psi(\vec{r})$ form [see Figs. 1(a) and 1(b)]. For $\bar{\psi} \neq 0$, the concentration shows a well-shaped distribution with a slightly asymmetric profile around the defect core [Figs. 1(d) and 1(e)]. The corresponding volumetric strain

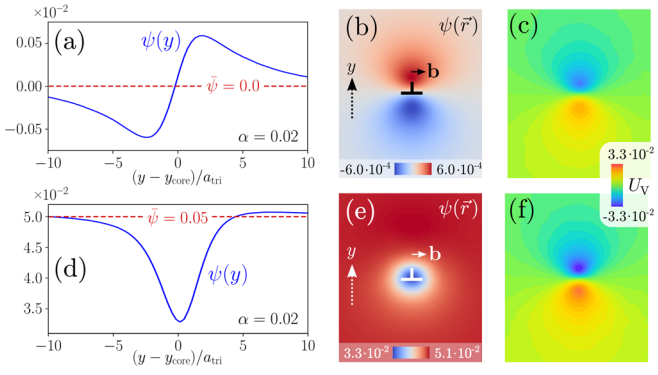

FIG. 1. Profiles of phase segregation and strain around a dislocation in a 2D triangular crystal with $\vec{b} = (b_x, 0)$: (a)–(c) $\psi(y - y_{\mathrm{core}})$, $\psi(\vec{r})$, and $U_V = U_{xx} + U_{yy}$ distributions for $\alpha = 0.02$ and $\bar{\psi} = 0$; (d)–(f) $\psi(y - y_{\mathrm{core}})$, $\psi(\vec{r})$, and U_V distributions for $\alpha = 0.02$ and $\bar{\psi} = 0.05$.

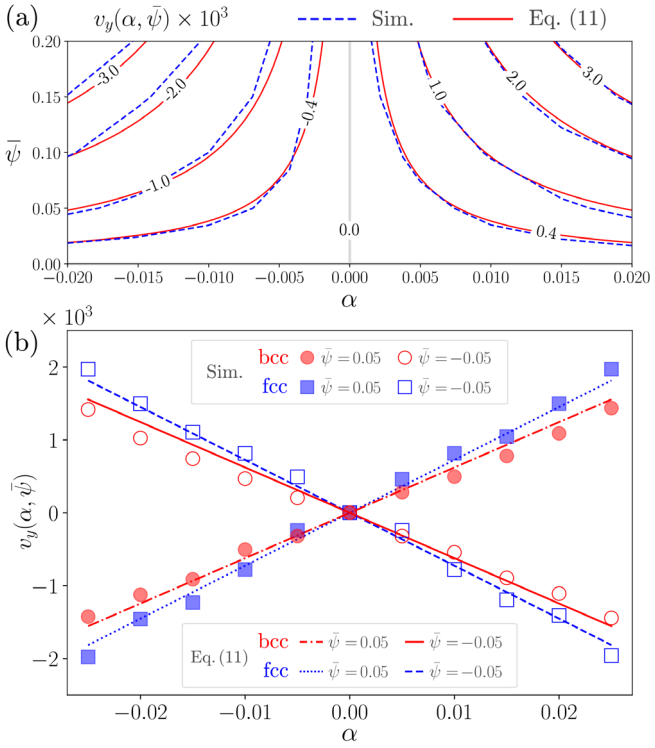

FIG. 2. Segregation-induced dislocation velocity $v_y(\alpha,\bar{\psi})$ evaluated from APFC simulations and the analytic result Eq. (11), for (a) triangular and (b) bcc and fcc symmetries.

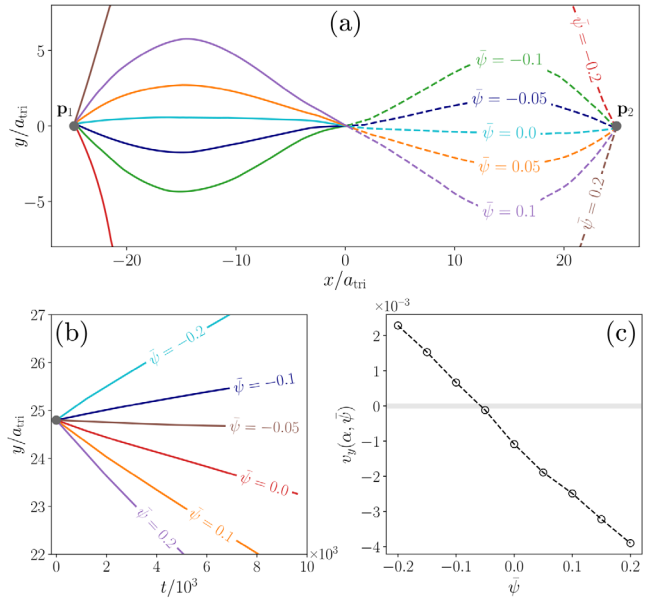

FIG. 3. (a) Trajectories of two 2D edge dislocations in the G configuration, for $\alpha=0.02$ and various values of $\bar{\psi}$, with $\bar{\psi}=0$ corresponding to pure glide. (b) Time evolution of the y position of the upper dislocation in configuration C with $\alpha=0.02$. $\bar{\psi}=0$ corresponds to pure climb. (c) Dislocation velocity as a function of $\bar{\psi}$ as identified from (b).

field $U_V=U_{xx}+U_{yy}$, which accounts for both lattice distortion and compositional strain (see Supplemental Material [39]), is reported in Figs. 1(c) and 1(f). Notice that for $\bar{\psi}=0$ the segregation slightly opposes the lattice deformation induced by the defect. For $\bar{\psi}=0.05$, the solute depletion at the core is observed, while an asymmetric contribution is present that resembles the effect observed for $\bar{\psi}=0$.

As described by Eq. (11) or (13), the preferential segregation (i.e., Cottrell atmospheres) at dislocations affects the defect velocity, with quantitative effects depending on the lattice symmetry. For the triangular case, the velocities $v_y^T(\alpha,\bar{\psi})$ obtained by simulations [Fig. 2(a), blue dashed lines] match well with the prediction of Eq. (14) [Fig. 2(a), red solid lines] with $\delta\psi$ extracted from simulations. Note that the velocity values in Fig. 2 have been subtracted by a small correction $v_y(0,0)$. This small drift is caused by the weak anisotropy in APFC Eq. (3) for displacements with the same magnitude but different sign [49]. It is not included in Eq. (13) and is found to be independent of α and $\bar{\psi}$. The velocities of dislocations in bcc and fcc crystals, forming between layers with opposite deformations u_x (see Supplemental Material [39]), are also calculated by both numerical simulations and Eq. (11), showing a good agreement as well, as demonstrated in Fig. 2(b). In these 3D cases, we have set the lattice displacements to obtain edge dislocations parallel to the z axis and $\vec{b}^s=b_x^s\hat{x}^s$, with $\hat{x}^B=[100]$, $b_x^B=2\pi\sqrt{2}$ (bcc), $\hat{x}^F=[110]$, and $b_x^F=\pi\sqrt{6}$ (fcc). The simulation results verify the linear dependence of dislocation velocity on the compositional strain or stress as predicted by Eq. (11).

More insights on the effects predicted by Eqs. (11) and (13) can be obtained by focusing on nonequilibrium configurations involving defect dynamics of glide and climb. For instance, we consider dislocation pairs in a triangular lattice that are expected to move by pure *glide* (G) and *climb* (C), with $\vec{b}_{1,2}=(\pm a_{\rm tri},0)$ and positions $(\pm d,0)$ and $(0,\pm d)$, respectively, in a $L\times L$ simulation box with $L\gg 2d$ and $d\sim 28a_{\rm tri}$. These configurations are initialized using the displacement field induced by straight edge dislocations [50] and the corresponding η_n [33] (see Supplemental Material [39]). The dynamics of these defects, depending on α and $\bar{\psi}$, is illustrated in Figs. 3(a)–3(c) for $\alpha=0.02$ and different values of $\bar{\psi}$. For configuration G, a nonzero v_y component is obtained, directly corresponding to the ones reported in Fig. 2(a), while a small but nonzero v_x encodes the effect of strain induced by the presence of a second dislocation, reproducing the effect of the Peach-Koehler force that leads to defect annihilation by pure glide in single-component systems. Interestingly, at relatively large values of $\alpha\bar{\psi}$, the annihilation of the dislocations by glide can be avoided [see Fig. 3(a) and Supplemental Videos [39]]. This new effect can be understood through Eq. (14): Given $|v_y^{t=0^+}|>|v_x^{t=0^+}|$, this absence of annihilation would occur

when $|\alpha\delta\psi| > |U_{xy}|/2$ with U_{xy} corresponding to the strain field component caused by the other dislocation in the dipole while $U_{xx}^{t=0^+} = U_{yy}^{t=0^+} = 0$. Therefore, as driven by purely thermodynamic driving forces, a threshold value exists for $|\alpha\delta\psi|$ above which the defect annihilation is prevented, with dislocations moving away from the traditional glide planes.

For configuration C, the velocity is oriented only along the y axis as predicted by Eq. (14) as $b_y = 0$. The symmetry of the simulations setup is such that the two dislocations are separated by $L_y/4$ (leaving them a distance $> 3L_y/4$ from their periodic counterpart). The contribution of compositional strain can then accelerate, slow down, or even prevent the annihilation, as illustrated in Figs. 3(b) and 3(c) (see also Supplemental Videos [39]). A change of the sign of the dislocation velocity is shown in Fig. 3(c), implying that the defects are moving toward their farther-away periodic counterpart. In this case, a threshold can be estimated through Eq. (14) again as the condition $v_y = 0$, yielding $\alpha\delta\psi = (3U_{xx} + U_{yy})/4$, with $U_{xy} = 0$.

A more complex configuration involving many defects is also examined, forming the dislocation network embedded in a crystalline matrix. In particular, we illustrate the case of a 3D bcc crystal with an embedded grain tilted by 10° about the [110] direction and of radius $\sim 15a_{\mathrm{bcc}}$ with $a_{\mathrm{bcc}} = 2\pi\sqrt{2}$ [32,51]. As illustrated in Fig. 4(a), a spherical network of dislocations, namely, a small-angle grain boundary, forms, and it is expected to shrink anisotropically [51–53]. The simulated solute segregation at defects is illustrated in Figs. 4(c) and 4(d). The rate of shrinkage of the dislocation network is affected by the solute expansion coefficient and average concentration [see Fig. 4(b)], which can be ascribed to the interplay of changes of defect dynamics as reported in Fig. 3. It is noted that analytic expressions (11) and (13) apply to straight dislocations. Extensions to arbitrarily curved dislocations in 3D, and, in turn, to configurations as in Fig. 4, are expected to follow by accounting for the local orientation of curved dislocation lines and the corresponding distortion in the lattice, e.g., through the use of the Nye tensor [54,55]. This formalism is being developed for single-component systems and will be extended to binary alloys.

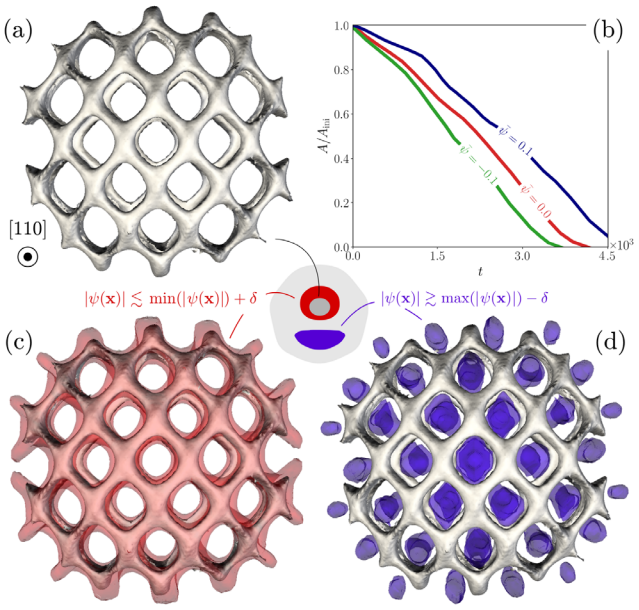

FIG. 4. (a) A network of dislocations at the boundary of an inclusion rotated by 10° about the [110] direction in a bcc crystal [regions shown: $\Phi < 0.85\max(\Phi)$]. (b) Normalized area of the grain boundary as a function of time, for $\alpha = 0.02$. (c),(d) Concentration segregation at defects for the dislocation network of (a). The middle inset shows spatial profiles of quantities of (a), (c), and (d) in a defect cross section.

In conclusion, through a coarse-grained approach we have identified analytic expressions for the velocities of dislocations in binary systems. The results predict the effects of compositional stress generated by the solute preferential segregation near the dislocation cores (i.e., Cottrell atmospheres) for different 2D and 3D crystalline symmetries, as confirmed by numerical simulations of the APFC model. While the influence of solute concentration on the magnitude of dislocation velocity was expected, this work also predicts some novel, segregation-induced behaviors of defect dynamics, such as the velocity components parallel to the Burgers vector in glide, leading to deflections from the traditional glide planes that could avert defect annihilation, as well as altering of the dislocation climb rate, reverse of climb direction, or even stagnation. The mesoscopic formulation constructed here provides a powerful tool to understand the nature of defect motion in binary alloys which controls the structural dynamics and properties of the material system.

We gratefully acknowledge the computing time granted by Jülich Supercomputing Centre (JSC) within Project No. HDR06 and by ZIH at TU Dresden. M. S. acknowledges support from the Emmy Noether Program of the German Research Foundation (DFG) under Grant No. SA4032/2-1. A. V. acknowledges support from the German Research Foundation (DFG) within SPP1959 under Grant No. VO899/19-2. K. R. E. acknowledges support from the National Science Foundation (NSF) under Grant No. DMR-1506634. The authors acknowledge useful discussions with N. Ofori-Opoku, V. Heinonen, L. Angheluta, and J. Viñals.

*marco.salvalaglio@tu-dresden.de

[1] G. Herzer, Modern soft magnets: Amorphous and nanocrystalline materials, Acta. Mater. **61**, 718 (2013).
[2] D. Xue, G. Chai, X. Li, and X. Fan, Effects of grain size distributions on coercivity and permeability of ferromagnets, J. Magn. Magn. Mater. **320**, 1541 (2008).

[3] S. Yip, The strongest size, Nature (London) **391**, 532 (1998).
[4] N. J. Petch, The cleavage strength of polycrystals, J. Iron Steel Inst. **174**, 25 (1953).
[5] Z. Fan, P. Hirvonen, L. F. C. Pereira, M. M. Ervasti, K. R. Elder, D. Donadio, A. Harju, and T. Ala-Nissila, Bimodal grain-size scaling of thermal transport in polycrystalline graphene from large-scale molecular dynamics simulations, Nano Lett. **17**, 5919 (2017).
[6] A. H. Cottrell, M. A. Jaswon, and N. F. Mott, Distribution of solute atoms round a slow dislocation, Proc. R. Soc. A **199**, 104 (1949).
[7] A. H. Cottrell and B. A. Bilby, Dislocation theory of yielding and strain ageing of iron, Proc. Phys. Soc. Sect. A **62**, 49 (1949).
[8] A. H. Cottrell, *Dislocations and Plastic Flow in Crystals*, International Series of Monographs on Physics (Clarendon, Oxford, 1953).
[9] K. Lücke and K. Detert, A quantitative theory of grain-boundary motion and recrystallization in metals in the presence of impurities, Acta Metall. **5**, 628 (1957).
[10] J. W. Cahn, The impurity-drag effect in grain boundary motion, Acta Metall. **10**, 789 (1962).
[11] K. Lücke and H. Stüwe, On the theory of impurity controlled grain boundary motion, Acta Metall. **19**, 1087 (1971).
[12] M. Hillert and B. Sundman, A treatment of the solute drag on moving grain boundaries and phase interfaces in binary alloys, Acta Metall. **24**, 731 (1976).
[13] M. Hillert, Solute drag in grain boundary migration and phase transformations, Acta Mater. **52**, 5289 (2004).
[14] J. W. Cahn, Thermodynamic aspects of Cottrell atmospheres, Philos. Mag. **93**, 3741 (2013).
[15] J. P. Hirth, On definitions and assumptions in the dislocation theory for solid solutions, Philos. Mag. **94**, 3162 (2014);
J. W. Cahn, Reprise: Partial chemical strain dislocations and their role in pinning dislocations to their atmospheres, Philos. Mag. **94**, 3170 (2014); J. P. Hirth, Response to comments, Philos. Mag. **94**, 3177 (2014).
[16] Y. Mishin and J. W. Cahn, Thermodynamics of Cottrell atmospheres tested by atomistic simulations, Acta Mater. **117**, 197 (2016).
[17] J. P. Hirth, D. M. Barnett, and R. G. Hoagland, Solute atmospheres at dislocations, Acta Mater. **131**, 574 (2017).
[18] H. Yoshinaga and S. Morozumi, The solute atmosphere round a moving dislocation and its dragging stress, Philos. Mag. A **23**, 1367 (1971).
[19] S. Takeuchi and A. S. Argon, Glide and climb resistance to the motion of an edge dislocation due to dragging a Cottrell atmosphere, Philos. Mag. A **40**, 65 (1979).
[20] F. Zhang and W. A. Curtin, Atomistically informed solute drag in Al–Mg, Model. Simul. Mater. Sci. Eng. **16**, 055006 (2008).
[21] R. B. Sills and W. Cai, Solute drag on perfect and extended dislocations, Philos. Mag. **96**, 895 (2016).
[22] Y. Gu and J. A. El-Awady, Theoretical framework for predicting solute concentrations and solute-induced stresses in finite volumes with arbitrary elastic fields, Materials Theory **4**, 1 (2020).
[23] Y. Mishin, Solute drag and dynamic phase transformations in moving grain boundaries, Acta Mater. **179**, 383 (2019).
[24] R. K. Koju and Y. Mishin, Direct atomistic modeling of solute drag by moving grain boundaries, Acta Mater. **198**, 111 (2020).
[25] R. Darvishi Kamachali, A. K. da Silva, E. McEniry, D. Ponge, B. Gault, J. Neugebauer, and D. Raabe, Segregation-assisted spinodal and transient spinodal phase separation at grain boundaries, npj Comput. Mater. **6**, 191 (2020).
[26] A. Rollett, G. Rohrer, and R. Suter, Understanding materials microstructure and behavior at the mesoscale, MRS Bull. **40**, 951 (2015).
[27] K. R. Elder, M. Katakowski, M. Haataja, and M. Grant, Modeling Elasticity in Crystal Growth, Phys. Rev. Lett. **88**, 245701 (2002).
[28] K. R. Elder and M. Grant, Modeling elastic and plastic deformations in nonequilibrium processing using phase field crystals, Phys. Rev. E **70**, 051605 (2004).
[29] K. R. Elder, N. Provatas, J. Berry, P. Stefanovic, and M. Grant, Phase-field crystal modeling and classical density functional theory of freezing, Phys. Rev. B **75**, 064107 (2007).
[30] A. Skaugen, L. Angheluta, and J. Viñals, Dislocation dynamics and crystal plasticity in the phase-field crystal model, Phys. Rev. B **97**, 054113 (2018).
[31] A. Skaugen, L. Angheluta, and J. Viñals, Separation of Elastic and Plastic Timescales in a Phase Field Crystal Model, Phys. Rev. Lett. **121**, 255501 (2018).
[32] M. Salvalaglio, A. Voigt, and K. R. Elder, Closing the gap between atomic-scale lattice deformations and continuum elasticity, npj Comput. Mater. **5**, 48 (2019).
[33] M. Salvalaglio, L. Angheluta, Z.-F. Huang, A. Voigt, K. R. Elder, and J. Viñals, A coarse-grained phase-field crystal model of plastic motion, J. Mech. Phys. Solids **137**, 103856 (2020).
[34] N. Goldenfeld, B. P. Athreya, and J. A. Dantzig, Renormalization group approach to multiscale simulation of polycrystalline materials using the phase field crystal model, Phys. Rev. E **72**, 020601(R) (2005).
[35] B. P. Athreya, N. Goldenfeld, and J. A. Dantzig, Renormalization-group theory for the phase-field crystal equation, Phys. Rev. E **74**, 011601 (2006).
[36] K. R. Elder, Z.-F. Huang, and N. Provatas, Amplitude expansion of the binary phase-field-crystal model, Phys. Rev. E **81**, 011602 (2010).
[37] Z.-F. Huang, K. R. Elder, and N. Provatas, Phase-field-crystal dynamics for binary systems: Derivation from dynamical density functional theory, amplitude equation formalism, and applications to alloy heterostructures, Phys. Rev. E **82**, 021605 (2010).
[38] In the original binary PFC model [29], the free energy contains terms $n(1+\nabla^2)^2 n$ and $\psi n\nabla^2(1+\nabla^2)n$, which transform in the amplitude formulation to $2\sum|\mathcal{G}_n\eta_n|^2$ and $-\sum(\eta_n\mathcal{G}_n^*\eta_n^* + \text{c.c.})\psi$ for 2D triangular and 3D bcc systems, respectively, requiring modes of only one length scale ($|\vec{q}_n| = 1$). For 2D square and 3D fcc lattices, two modes are needed, and it is convenient to use $n[q_1^2/(q_1^2-1)]^2(1+\nabla^2)^2(1+\nabla^2/q_1^2)^2 n$ and $[q_1^2/(q_1^2-1)]^2\psi n\nabla^2(1+\nabla^2)\times(1+\nabla^2/q_1^2)(q_1^2+1+2\nabla^2)$, which then transform to

$2\sum|\mathcal{G}_n\eta_n|^2$ and $-\sum q_n^2(\eta_n\mathcal{G}_n^*\eta_n^* + \text{c.c.})\psi$, respectively, where q_1 corresponds to the other length scale.

[39] See Supplemental Material at http://link.aps.org/supplemental/10.1103/PhysRevLett.126.185502 for the discretization scheme and the setups of initial conditions for numerical simulations, the expressions of dislocation velocity for various crystalline symmetries, the expressions of the compositional contribution to strain and stress for binary alloys, and some videos of dislocation motion, which includes Ref. [40].

[40] W. Cai, A. Arsenlis, C. R. Weinberger, and V. V. Bulatov, A non-singular continuum theory of dislocations, J. Mech. Phys. Solids **54**, 561 (2006).

[41] Z.-F. Huang, Scale-coupling and interface-pinning effects in the phase field crystal model, Phys. Rev. E **87**, 012401 (2013); Z.-F. Huang, Scaling of alloy interfacial properties under compositional strain, Phys. Rev. E **93**, 022803 (2016).

[42] V. Heinonen, C. V. Achim, K. R. Elder, S. Buyukdagli, and T. Ala-Nissila, Phase-field-crystal models and mechanical equilibrium, Phys. Rev. E **89**, 032411 (2014).

[43] V. A. Lubarda, Dislocation Burgers vector and the Peach–Koehler force: A review, J. Mater. Res. Technol. **8**, 1550 (2019).

[44] L. D. Landau and E. M. Lifshitz, *Theory of Elasticity*, 2nd ed. (Pergamon, Oxford, 1970).

[45] S. Vey and A. Voigt, AMDiS: Adaptive multidimensional simulations, Comput. Visual. Sci. **10**, 57 (2007).

[46] T. Witkowski, S. Ling, S. Praetorius, and A. Voigt, Software concepts and numerical algorithms for a scalable adaptive parallel finite element method, Adv. Comput. Math. **41**, 1145 (2015).

[47] M. Salvalaglio, R. Backofen, A. Voigt, and K. R. Elder, Controlling the energy of defects and interfaces in the amplitude expansion of the phase-field crystal model, Phys. Rev. E **96**, 023301 (2017).

[48] S. Praetorius, M. Salvalaglio, and A. Voigt, An efficient numerical framework for the amplitude expansion of the phase-field crystal model, Model. Simul. Mater. Sci. Eng. **27**, 044004 (2019).

[49] C. Hüter, M. Friák, M. Weikamp, J. Neugebauer, N. Goldenfeld, B. Svendsen, and R. Spatschek, Nonlinear elastic effects in phase field crystal and amplitude equations: Comparison to *ab initio* simulations of BCC metals and graphene, Phys. Rev. B **93**, 214105 (2016).

[50] P. Anderson, J. Hirth, and J. Lothe, *Theory of Dislocations* (Cambridge University Press, Cambridge, England, 2017).

[51] M. Salvalaglio, R. Backofen, K. R. Elder, and A. Voigt, Defects at grain boundaries: A coarse-grained, three-dimensional description by the amplitude expansion of the phase-field crystal model, Phys. Rev. Mater. **2**, 053804 (2018).

[52] R. Doherty, D. Hughes, F. Humphreys, J. Jonas, D. Jensen, M. Kassner, W. King, T. McNelley, H. McQueen, and A. Rollett, Current issues in recrystallization: A review, Mater. Sci. Eng. A **238**, 219 (1997).

[53] A. Yamanaka, K. McReynolds, and P. W. Voorhees, Phase field crystal simulation of grain boundary motion, grain rotation and dislocation reactions in a BCC bicrystal, Acta Mater. **133**, 160 (2017).

[54] J. Nye, Some geometrical relations in dislocated crystals, Acta Metall. **1**, 153 (1953).

[55] C. Hartley and Y. Mishin, Characterization and visualization of the lattice misfit associated with dislocation cores, Acta Mater. **53**, 1313 (2005).